Summer 7-11-2019

III-V nBn Focal Plane Arrays: Radiometric Characteristics as a Function of Detector Cutoff Wavelength

Victor Darie Pepel

Victor D. Pepel

Candidate

Electrical and Computer Engineering (ECE)

Department

This dissertation is approved, and it is acceptable in quality and form for publication:

Approved by the Dissertation Committee:

Dr. Ganesh Balakrishnan, Chairperson

Dr. Payman Zarkesh-Ha

Dr. Jane Lehr

Dr. Christian Morath

III-V *nBn* Focal Plane Arrays: Radiometric Characteristics as a Function of Detector Cutoff Wavelength

by

Victor D. Pepel

B.S., Elect. Engineering, Oregon Inst. of Technology, 2017

THESIS

Submitted in Partial Fulfillment of the
Requirements for the Degree of

Master of Science
Electrical Engineering

The University of New Mexico

Albuquerque, New Mexico

July, 2019

III-V *nBn* Focal Plane Arrays: Radiometric Characteristics as a Function of Detector Cutoff Wavelength

by

Victor D. Pepel

B.S., Elect. Engineering, Oregon Inst. of Technology, 2017

MS., Engineering, University of New Mexico, 2019

ABSTRACT

Summarized here are the measured radiometric characteristics of three Infrared III-V InAsSb/AlAsSb/InAsSb-based *nBn* focal plane arrays (FPAs) in the SWIR to MWIR range with cutoff wavelengths of 2.85 µm, 3.3 µm and 4.2 µm at the nominal operating temperature of 150 K. Herein referred to by their respective cutoff wavelengths, the *nBn* detectors are characterized across the temperature range of 130 K to 180 K. The optical response and noise characteristics are examined as a function of cutoff wavelength, and a comparison of dark current density is made to HgTeCd photodiodes using the Rule ‘07 heuristic.

The 2.85 µm, 3.3 µm and 4.2 µm *nBn* detectors demonstrated quantum efficiencies of 25%, 68% and 82% respectively at the nominal operating temperature of 150 K. The relatively low quantum efficiency observed on the lower cutoff wavelength detectors suggests a lower carrier lifetime due to an increased number of mid gap trap states. Other

radiometric metrics such as noise equivalent irradiance (NEI) and responsivity are analyzed as a function of temperature and detector bias, and noise models are created to quantize the effect of various noise components on the overall performance of the detector. An Arrhenius analysis of the dark current data is performed and the activation energies for the *nBn* detectors provide insight into the dominant dark current mechanisms and possible detector defects, such as the existence of a depletion region in the lower cutoff detectors and the existence of a valence band offset in the 4.2 μm detector. The III-V *nBn* detectors displayed higher dark current densities compared to their theoretical HgCdTe counterparts, especially at low temperatures. However, results indicate an ongoing improvement in III-V *nBn* dark current compared to previous years. In all the metrics considered, a lower cutoff wavelength was associated with a decrease in performance for the *nBn* detectors, except for the bias operating range where the 4.2 μm cutoff FPA displayed more stringent biasing requirements compared to the lower cutoff FPAs.

TABLE OF CONTENTS

LIST OF FIGURES

FIGURE PAGE

LIST OF TABLES

Chapter 1

Introduction

1.1 Infrared Focal Plane Arrays

Otherwise known as sensor chip assembly (SCA), a focal plane array (FPA) refers to a collection of detector pixels mounted in a periodic 2-dimensional arrangement at the focal plane of an optical system. FPAs operating in the infrared spectrum can be used in military applications for missile guidance systems, missile detection and reconnaissance applications, as well as for geographic and other data-collection purposes.

An FPA consists of two distinct elements: (1) the detector array made from infrared material such as HgCdTe or InAsSb which converts incoming photons to electrical charge carriers; and, (2), the silicon-based read out integrated circuit (ROIC), which is directly bonded to the detector array and amplifies the electrical signals from it, as well as providing the timing, digitization and transmission of the data. Each pixel of the FPA thus consists of detector material and the Si unit cell that provides the charge integration across the integration capacitors and allows the optical charge to be sampled by an analog to digital converter (ADC). An FPA can have an ADC for each individual pixel, or it can have ADCs strategically placed on each row or column of the FPA in order to decrease

costs, power dissipation and space requirements. Figure 1 depicts a common detector and ROIC configuration [1].

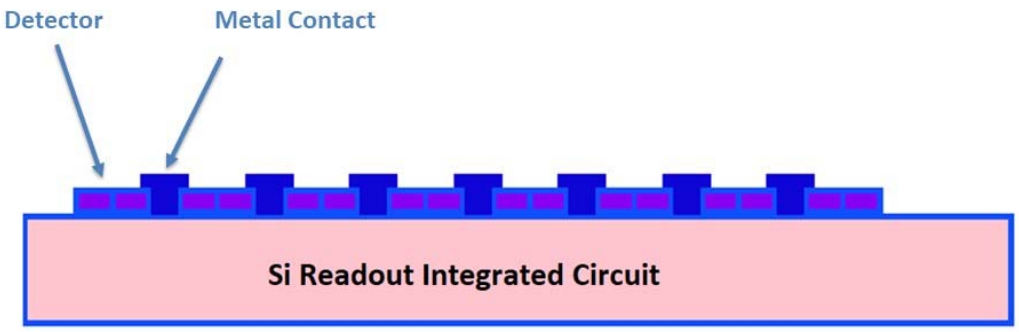

Figure 1. FPA consisting of detector material, metal interface and Silicon Readout. Credit: John E. Hubbs.

1.2 *nBn* Detector Architecture

Traditionally HgCdTe SCAs have dominated space-based applications due to their high radiation tolerance, high quantum efficiency and low dark current [2], however, a new class of detectors termed *nBn* detectors was proposed in 2006 by Maimon and Wicks [3] which displays lower dark current than traditional III-V photodiodes and is easier and less expensive to manufacture than HgCdTe photodiodes. The band gap structure of the *nBn* architecture is presented in Figure 2. It consists of an n-type absorber region, a large band gap barrier layer and a second n-type layer that serves as simply a contact layer. The barrier serves to block the flow of majority electron carriers while allowing the flow of minority hole carriers. The *nBn* architecture serves to reduce two sources of dark current: (1) dark current associated with the generation-recombination process in a depletion region, due to the abundance of Shockley-Reed-Hall (SRH) centers; and (2), dark current

associated with surface currents on the detector, which arise from Fermi-level pinning in the conduction band at the surface of the detector. The lower dark current of the *nBn* would ideally allow them detectors to operate at higher temperatures without losing performance in the noise characteristics of the detector compared to its III-V photodiode counterparts. However, despite the advantages of the *nBn* architecture to traditional photodiodes, current *nBn* devices have suffered from comparatively high dark current and low quantum efficiency due to lower than expected carrier lifetime and diffusion length, and are generally still outperformed by II-VI HgCdTe photodiodes grown lattice matched on CdZnTe substrate [3,4]. As a relatively new technology, the *nBn* architecture has progressed since its inception and may still reach the level of development that will provide advantages in terms of noise characteristics and operating temperatures to traditional HgCdTe photodiodes.

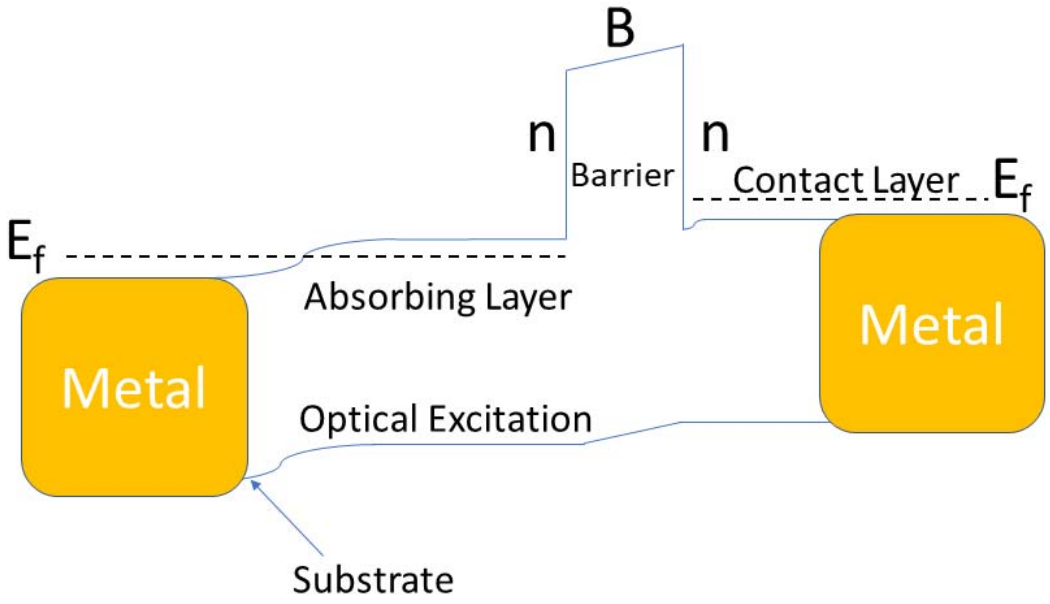

Figure 2. *nBn* detector architecture biased under normal operating conditions

The three main dark current components in photodiodes based on narrow band gap semiconductors are as follows [3]:

(1) Generation-Recombination or depletion dark current that gets generated in the depletion region of pn junction photodiodes, J_{depl}.

(2) Diffusion current associated with recombination processes in the extrinsic area of the photodetector, J_{diff}.

(3) Surface current J_{surf} which mainly depends on the passivation process implemented on the detector.

In the ideal case, the *nBn* architecture effectively eliminates the first and third component. There is ideally no depletion current generated by generation-recombination due to the n-type layer operating in near flatband, thus creating an insignificant depletion region. The depletion current is given by the following expression:

$$J_{Depl} = q\frac{n_i}{\tau_g}W_{dep}, \tag{1.1}$$

where q is the electrical charge, n_i is the intrinsic carrier density, W_{dep} is the depletion width and τ_g is the generation lifetime. When width of the depletion region is near zero, as in ideal *nBn* detectors, the depletion current is minimized. Due to the dependence of the depletion current on n_i, the dark current generated by this process has an activation energy of $E_g/2$, or half of the band gap [3,5].

The diffusion current is dependent n_i^2 and has an activation energy equal to the band gap. In the typical case where the diffusion length is long compared to the absorber width, the diffusion current in an *nBn* is given by the following expression:

$$J_{Diff} = q\frac{ni^2}{N_d\tau_r}L, \tag{1.2}$$

where N_d is the doping concentration, τ_r is the recombination lifetime, and L is the width of the neutral absorbing region [3]. The recombination lifetime is given by the following:

$$\frac{1}{\tau_r} = \frac{1}{\tau_{AUG}} + \frac{1}{\tau_{RAD}} + \frac{1}{\tau_{SRH}}, \tag{1.3}$$

where τ_{AUG} is the Auger lifetime, τ_{RAD} is the radiative lifetime and τ_{SRH} is the Shockley-Reed-Hall lifetime. An excellent discussion about lifetime in semiconductors is given by Schroder in [6]. Under the assumption of a single recombination level, which is sufficient for illustrative purposes, the generation lifetime is related to the recombination lifetime by the following:

$$\frac{\tau_g}{\tau_r} = e^{\frac{E_t - E_i}{kT}}, \tag{1.4}$$

where E_t is the trap energy and E_i is the intrinsic fermi level, k is the Boltzman constant and T is the temperature. By examining the activation energy of the dark current in the detector, the dominant source of dark current can be determined.

1.3 Read-Out Integrated Circuit and Unit Cell Architecture

When characterizing the performance metrics of FPAs it is important to consider not only the detector materials and architecture, but the characteristics of the ROIC and the unit cell architecture. There are several type of unit cell architectures that provide different types of advantages. The four basic types of unit cells for photovoltaic detectors are: (1) Source Follower Per Detector (SFD); (2) Direct Injection (DI); (3) Feedback Enhance

Direct Injection (FEDI); and, (4) the Capacitor Feedback Transimpedance Amplifier (CTIA). An excellent discussion on the operations of the various types of unit cells is given by P. Norton [2]. More detail will be provided on the DI unit cell since this is the type of architecture implemented on the FPAs characterized in this work. Shown in Figure 3 is the DI unit cell. The current from the detector charges the C_{int} capacitor for the duration of the integration time. The charge is also stored on the "sample and hold" capacitor labeled $C_{S/H}$. The sample and hold capacitor allows for the functioning of the FPA in a integrate while read mode, which increases operating speed by allowing the digitization of the voltage data to be done on $C_{S/H}$ while the C_{int} capacitor integrates the charge for a new frame. V_{RST} allows the emptying of the capacitors between frames, and the switch between the two capacitor allows for their seclusion in order to sustain the Integrate While Read capability. The switch labeled SW_{ADC} allows for the multiplexing of the capacitor charge from different pixels located on a column of the FPA to an ADC located on the column bus, which handles the digitization for all the pixels on the column. The size of the capacitors affects the full well capacity of the detector and the conversion gain of electrons to digital counts. This is because smaller capacitors will show a larger swing in voltage for a given increase in charge, making it easier for the ADC to detect small changes in optical signal strength:

$$V = \frac{q}{C}, \tag{1.5}$$

where V is the voltage across the capacitor, q is the electron charge in coulombs and C is the capacitance in farads. The DI unit cell is well suited to irradiance levels on the scale of 10^{12} ph/s-cm^2, but it is not recommended for low irradiance levels or detectors with low R_0A products due to decreases in the injection efficiency of the amplifier. R_0A is the

product of the detector impedance under zero bias and the detector active area. Low R_0A products are found in detectors with high dark current, and the R_0A product decreases as a function of cutoff wavelength [2]. Therefore, dark current characteristics to be presented may be impacted by the unit cell architecture, and may not be solely reflective of detector performance, especially for the 4.2 µm FPA.

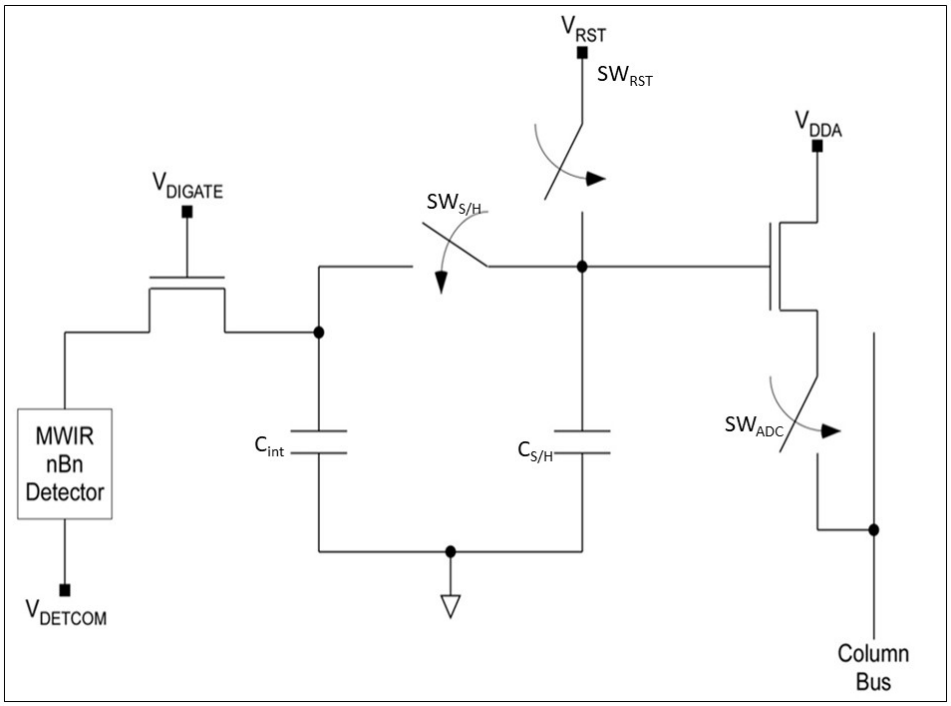

Figure 3. Unit cell diagram containing Direct Injection FET

1.4 *nBn Focal Plane Array Device Description*

The detectors characterized in this work use an III-V InAsSb/AlAsSb/InAsSb-based *nBn* architecture with a ternary absorber region. The cutoff wavelengths at 150 K are approximately 2.85 µm for the E-SWIR, while in the MWIR region SCAs at two different cutoff wavelengths were examined: 3.3 µm and 4.2 µm. The SCAs are bonded

to the Digital Read Out Integrated Circuits (ROIC) which utilize the DI unit cell architecture.

The unit cell amplifier provides a full well capacity of 2 million electrons. The output from the amplifier is handled by sample-and-hold (S/H) circuitry to allow “snapshot” mode operation with variable integration time and integrate-while-read functionality. The on-chip analog-to-digital conversion has 14-bit resolution. The pixel data is then transmitted using low voltage differential signal (LVDS) output drivers.

The ROIC registers are programmable through a serial data interface. The serial data is used to set parameters of the ROIC such as integration time and detector bias, as well as control parameters for all other ROIC functions. There is also a serial output to read back the register data. The user must provide a master clock, serial commands, power, and ground connections to establish proper ROIC operation.

The ROIC has built-in analog and digital test bits (ABIT & DBIT) to allow monitoring of internal signals, such as the voltage applied across the detector. The test bits allow for precise optimization of SCA performance and increase its testability.

Chapter 2

Focal Plane Array Performance Metrics and Characteristics

2.1 Quantum Efficiency

In order to characterize the performance of the FPAs, a few key metrics were considered. The quantum efficiency (η) was calculated using the measured responsivity of the detector, the area of the detector (A_{Det}), the integration time (T_{int}), and the transimpedance (C_g). The quantum efficiency is a measure of how well the detector converts incident photons to collected electrons:

$$\eta = \frac{Responsivity}{A_{Det}T_{int}C_g}\left[\frac{electrons}{photon}\right]. \quad (2.1)$$

The responsivity was extracted from the slope of the median pixel output vs. photon irradiance curve:

$$Responsivity = \frac{d(Output)}{d(E_q)}\left[\frac{Counts}{photon/\sec - cm^2}\right]. \quad (2.2)$$

An example of the median pixel output measured at four different irradiance levels, ranging from 1 x 10^9 ph/s-cm^2 to 140 x 10^{12} ph/s-cm^2 is shown below in Figure 4.

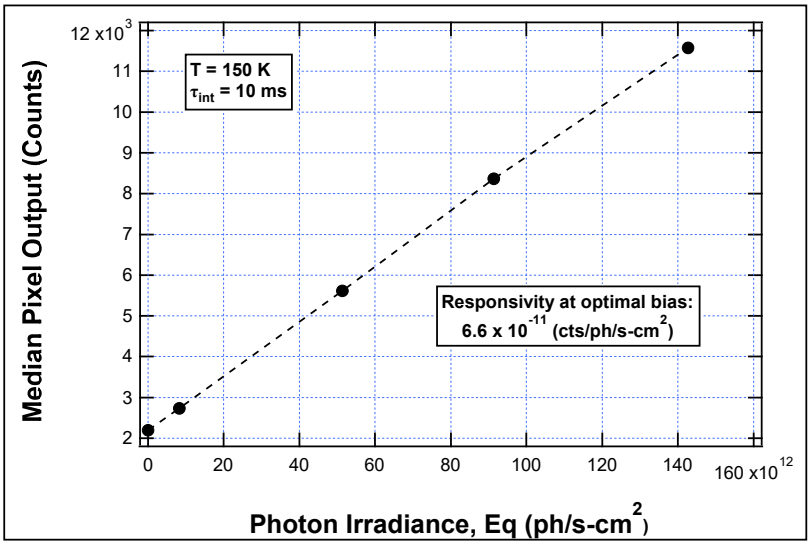

Figure 4. Example median pixel output vs. photon irradiance used for responsivity extraction

The conversion gain, unit cell transimpedance, or C_g, is extracted via standard variance analysis and quantifies the number of collected electrons required to increase the ADC output by one count [1,7,8]:

$$C_g = \frac{d(Output\ Variance)}{d(Output)}\left[\frac{Counts}{electron}\right]. \quad (2.3)$$

As an example, Figure 5 shows the median pixel variance vs. median pixel output curve used to extract the C_g value for the 3.3 µm SCA.

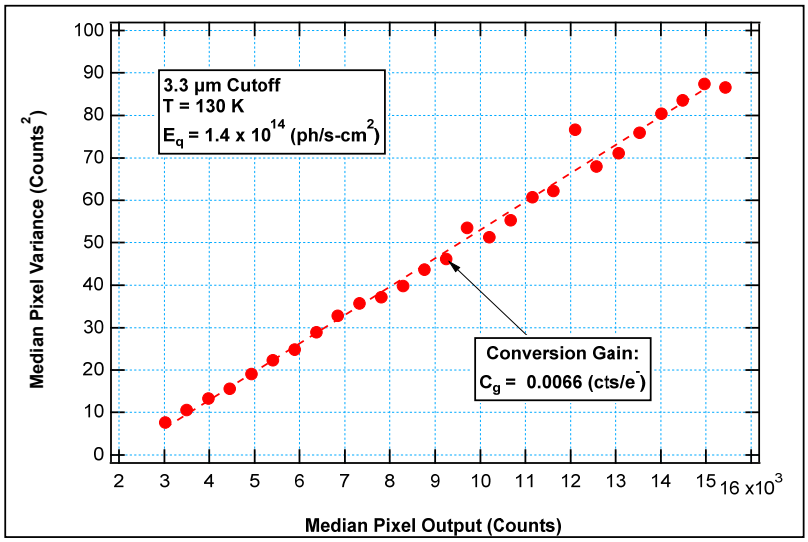

Figure 5. Example transimpedance extraction

2.2 Noise

The noise is calculated on a per-pixel basis as the standard deviation in detector digital output across 100 frames, and has units of RMS counts.

2.3 Noise Equivalent Irradiance

The NEI describes the amount of irradiance required to create a signal to noise ratio of unity, and is a measure of the sensitivity of the detector. This metric is obtained by dividing the median pixel noise by the median responsivity of the detector. The responsivity is calculated as the slope of output versus irradiance, whereas the noise is

calculated as the standard deviation of the pixels across 100 frames. This metric thus combines multiple parameters, such as responsivity, dark current and detector ROIC noise, into a single number that reflects the overall performance of the detector, and is useful for performance comparison across different detector types [2]:

$$NEI = \frac{RMS\ Noise\ [Counts]}{Responsivity\left[\frac{Counts}{photon/\sec - cm^2}\right]}\left[\frac{photons}{sec{-}cm^2}\right]. \quad (2.4)$$

2.4 Dark Current

The dark current is obtained by measuring the pixel output as a function of integration time, in conjunction with other parameters of the detector, as given below:

$$I_{dark} = \frac{q}{C_g}\left(\frac{dOutput}{dT_{int}} - C_g \eta E_q A_{Det}\right)[Amperes]. \quad (2.5)$$

For practical purposes, the second term is considered to be insignificant due to E_q = 1 x 10^9 ph/s-cm^2 for these measurements.

2.5 Noise Models

In order to quantify the impact of the various noise sources on the overall performance of the detector, the noise contribution from different sources can be calculated.

2.5.1 Photon Noise

As the random nature of the arrival times of incident photons creates fluctuations in the optical signal, this creates a noise source that is a function of the optical signal itself and cannot be reduced without reducing the optical response of the detector. The noise contribution from photons can be calculated as shown below.

$$\text{Photon Noise} = C_g\sqrt{E_q T_{int} A_{det}\eta} \qquad RMS\ Noise\ [Counts] \tag{2.6}$$

2.5.2 Detector Thermal Noise

The detector thermal noise is the noise generated by the dark current due to the random arrival times of charge carriers at the junction. It depends on the total quantity of charge produced by the dark current and the conversion gain.

$$\underset{\text{Thermal Noise}}{\text{Detector}} = C_g\sqrt{\frac{I_D T_{int}}{q}} \qquad RMS\ Noise\ [Counts] \tag{2.7}$$

2.5.3 ROIC Noise

The detector ROIC noise is due to the thermal noise of the MOSFETs, the 1/f noise of the MOSFETs and the transfer function of the signal processing circuit [8]. As the signal progresses through its electronic path, the noise contributions from each component get added in quadrature to the total ROIC noise. The detector ROIC noise is a constant value independent of irradiance value or integration time. This metric is not a function of detector performance, but a function of the unit cell and ROIC characteristics. At low irradiance values and integration times, the ROIC noise becomes the largest noise source. An approximate measurement of the ROIC noise can be obtained by measuring the pixel noise at low integration times and irradiance levels.

2.5.4 Total Noise

The total noise can be found by summing in quadrature the components discussed previously. If the calculations are performed correctly, the total noise should match the actual noise measured on the FPAs.

$$\text{Total Noise} = \sqrt{Photon^2 + ROIC^2 + Thermal^2} \;\; RMS\ Noise\ [Counts] \tag{2.8}$$

2.6 Activation Energy

The activation energy in the detector material can be obtained by performing an Arrhenius analysis on the dark current data. This requires plotting the measured dark current as a function of inverse temperature, and then performing an exponential fit to extract τ, the exponential fitting constant. The exponential fitting formula is shown below.

$$F = y_0 + Ae^{\frac{-(x-x0)}{\tau}} \tag{2.9}$$

Using the extracted τ value and k, the Boltzmann constant, the activation energy becomes:

$$E_{act} = \frac{k}{\tau} \;\; [eV] \tag{2.10}$$

The activation energies can be compared to the band gap of the absorber material in order to gain insights about the dominant recombination mechanisms and possible defects in the detectors. The band gap for the three cutoff wavelengths can be computed as shown below.

$$\text{Band Gap} = \frac{hc}{\lambda_c} \;\; [eV], \tag{2.11}$$

where h is the Planck constant, c is the speed of light in vacuum and λ_c is the cutoff wavelength. Using the above formulation, the band gaps for the 2.85 µm, 3.3 µm and 4.2 µm cutoff wavelengths are computed to be 0.435 eV, 0.376 eV and 0.295 eV respectively.

2.7 Rule ’07: A Heuristic Predictor of HgCdTe Photodiode Performance

When first introduced, the *nBn* architecture showed the potential to outperform HgCdTe photodiodes in terms of dark current characteristics. The Rule ’07 heuristic was introduced in 2008 as a convenient rule of thumb to estimate the dark current density in state-of-the-art HgCdTe photodiodes [9]. Using this heuristic, the expected dark current density of an equivalent cutoff wavelength HgCdTe photodiode detector can be computed and compared to the performance of the *nBn* detectors characterized in this experiment.

$$J = J_0 e^{C\left(\frac{1.24q}{k\lambda_e T}\right)} \quad \left[\frac{Amperes}{cm^2}\right] \tag{2.12}$$

$\lambda_e = \lambda_{cutoff}$ for $\lambda_{cutoff} > \lambda_{threshold}$

$$= \lambda_{cutoff}/\left[1 - \left(\frac{\lambda_{scale}}{\lambda_{cutoff}} - \frac{\lambda_{scale}}{\lambda_{threshold}}\right)^{Pwr}\right], \text{ for } \lambda_{cutoff} < \lambda_{threshold} \tag{2.13}$$

And the following constants were obtained experimentally by W.E. Tennant in [9].

$J_0 = 8367.00$ A/cm2; $C = -1.16$; $P_{wr} = 0.54$; $\lambda_{scale} = 0.20$; $\lambda_{threshold} = 4.64$µm.

2.8 Optimal Operating Bias

Some of the measurements shown in this work were performed at what was determined to be the optimal operating bias voltage. The optimal bias is an applied detector bias which yields high responsivity, quantum efficiency, and uniformity, while keeping the dark current value low. Selecting a reverse bias voltage stronger than the ideal bias would produce higher responsivity and higher quantum efficiency, but it would degrade the performance of the detector in terms of generating higher dark current and poor uniformity characteristics. Selecting a reverse bias that is weaker than the optimal bias would have the effect of reducing dark current and increasing uniformity, at the cost of lower responsivity and quantum efficiency.

The way to determine the bias which offers the optimal tradeoff between responsivity, quantum efficiency and dark current, is by examining the NEI curve as a function of applied detector bias at high irradiance values. Since the NEI is a composite metric which contains the responsivity in the denominator and the noise in the numerator, selecting an operating bias that minimizes the NEI will yield the desired tradeoff in terms of radiometric performance. As an illustrative example, Figure 6 shows the NEI vs. applied detector bias data used to determine the optimal bias voltage under nominal operating conditions for the 3.3 μm cutoff SCA. Highlighted is the optimal operating region, which consists of low NEI values obtained with a weak reverse bias voltage. Additionally, before selecting the optimal bias, the operability of the NEI must be verified to be high. NEI operability is defined as the percent of pixels that fall within 25% of the median NEI value. Having an NEI operability of 100% would imply that all the pixels in an array have NEI values that are within 25% of the median pixel NEI. Using NEI as the metric for

optimizing radiometric performance, and NEI operability as a measure of uniformity, an optimal bias can be selected. Preference is given to weak reverse bias voltages due to lower power dissipation and due to anticipated shifts in the NEI curve when the detectors are exposed to a high radiation environment for space-based applications.

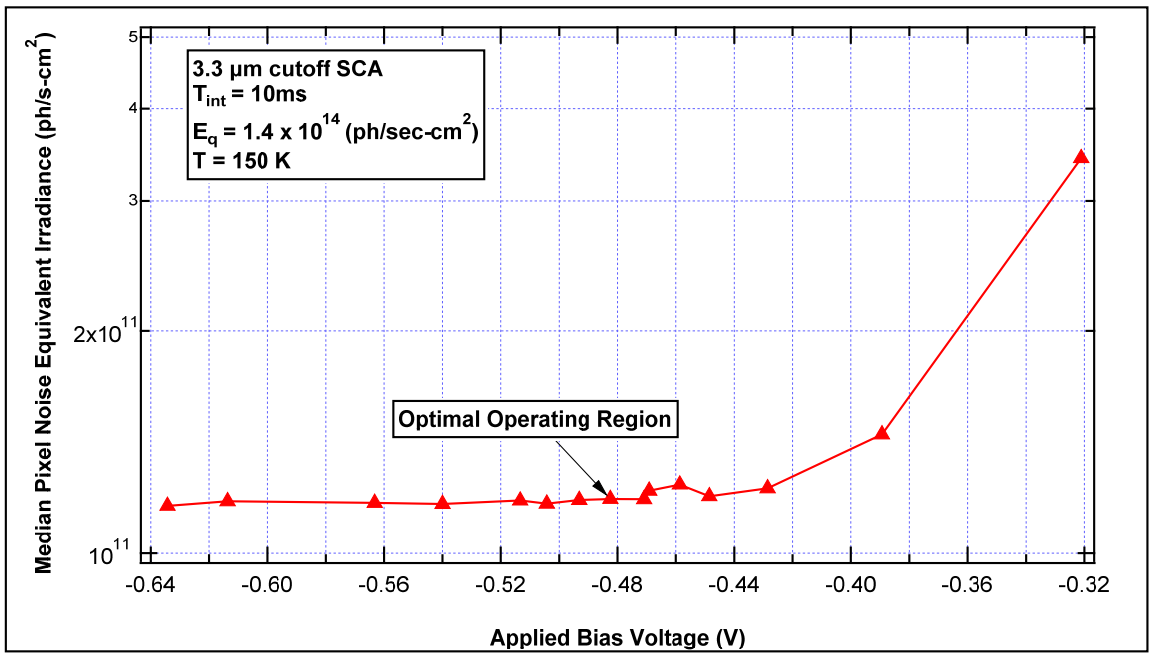

Figure 6. Example highlighting optimal bias region based on low NEI and low voltage magnitude

Chapter 3

Experimental Setup

3.1 Experimental Setup

The radiometric characterizations were completed under the following conditions: all SCAs were mounted in a liquid nitrogen pour-filled dewar and held at precise temperatures between 130 K and 180 K with a cryogenic temperature controller. The full field-of-view of the detectors was filled with a 4” plate blackbody source calibrated to the necessary temperature to provide the desired photon irradiances. The field-of-view of the detectors was set by small apertures mounted on the inner shield (at 77 K) as shown in Figure 7. The dewar was designed to house five apertures that could easily be swapped to provide a wide range of irradiances. The spectrum for characterization was controlled by optical bandpass filters that were mounted in the dewar near the limiting aperture at 77 K.

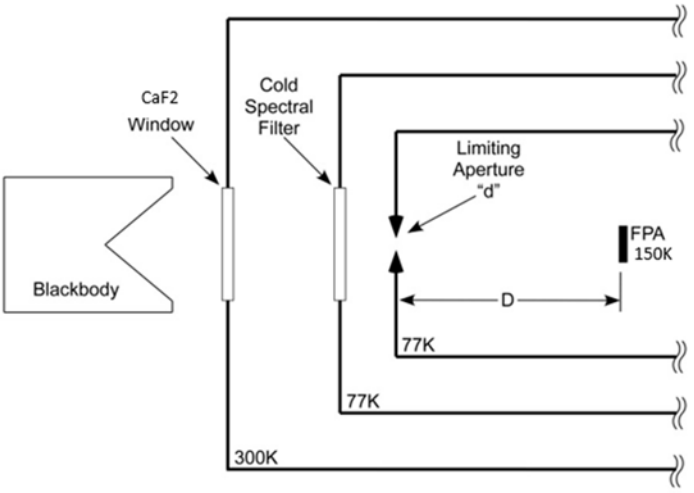

Figure 7. Radiometric configuration for SCA characterizations

The photon irradiances were calculated as follows:

$$E_q = \Omega \int_0^\infty L_q(\lambda, T)\, RRPH(\lambda)\tau_{window}(\lambda)\tau_{filter}(\lambda)d\lambda, \quad (3.1)$$

where:

$E_q(T)$ = photon irradiance (ph/s-cm^2)
$L_q(\lambda,T)$ = spectral photon radiance (ph/s-cm^2-sr-µm)
RRPH(λ) = detector relative photon spectral response
λ = wavelength (µm).
Ω = solid angle of the detector FOV (sr)
τ_{window} (λ) = transmittance of dewar window
τ_{filter} (λ) = transmittance of spectral filter

The 2.85 µm and 3.3 µm cutoff SCAs were measured using filter K, which has a center wavelength of 2.2 µm, while the 4.2 µm cutoff SCA was measured using filter W03311-6, which has a center wavelength of 3.3 µm. Figure 7 shows the transmission spectra of the two filters.

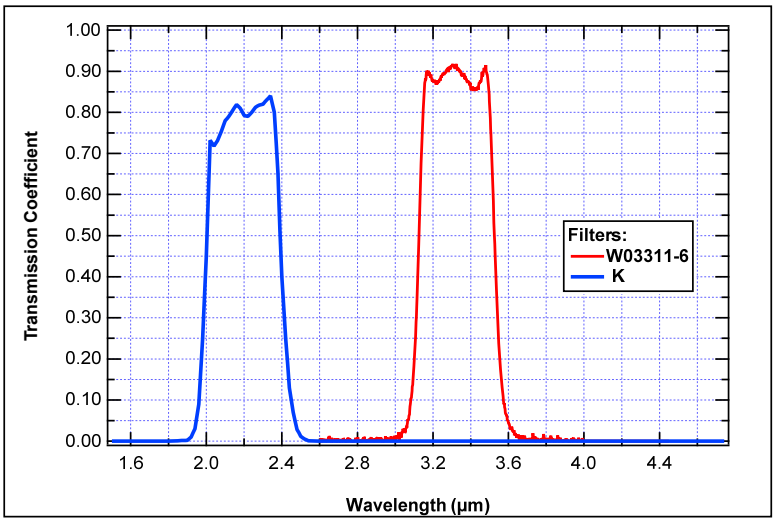

Figure 8: Filter transmission spectra. Filter K used for 2.85 µm and 3.3 µm SCAs; Filter W03311-6 used for 4.2 µm SCA

Chapter 4

FPA Characterization Results

4.1 Responsivity and Quantum Efficiency vs. Applied Detector Bias

The responsivity curves extracted at the nominal operating temperature of 150 K and integration time of 10 milliseconds are shown below in Figure 9 for every SCA cutoff wavelength as a function of applied detector bias. Responsivity was calculated from plots of output vs E_q according to equation 2.2.

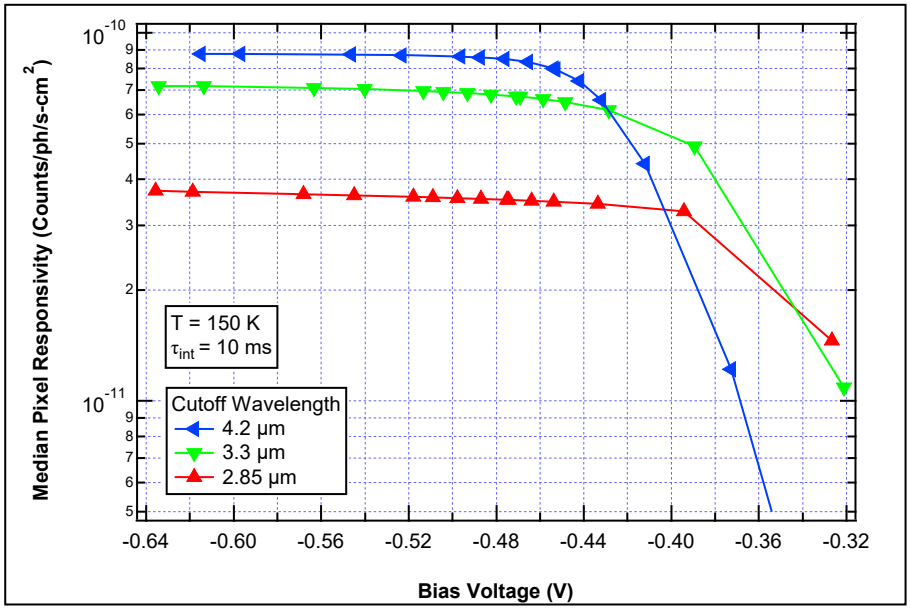

Figure 9. Median pixel responsivity vs. applied bias voltage for each SCA

Using the responsivity values extracted from the median pixel output vs. photon irradiance curves, the quantum efficiencies for every SCA as a function of applied bias voltage were calculated according to equation 2.1 and are displayed below in Figure 10.

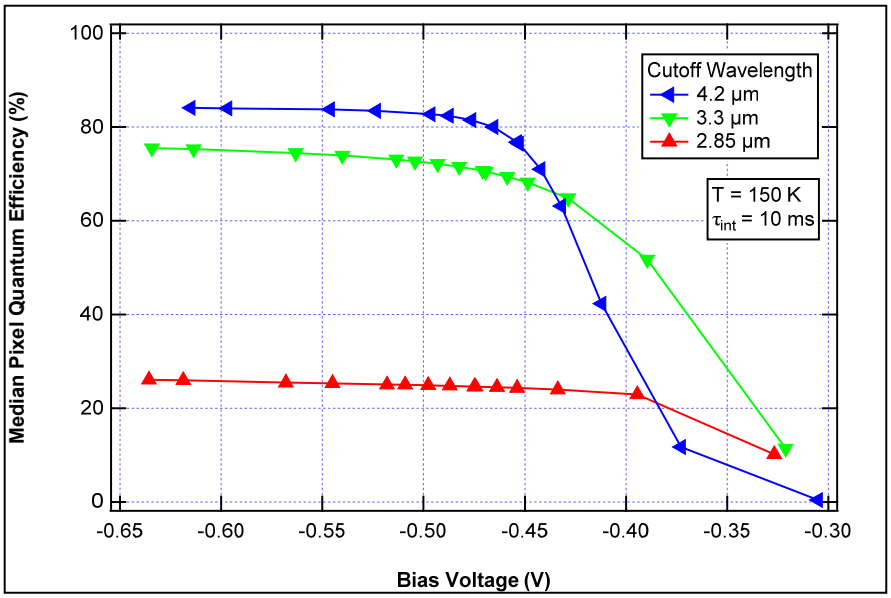

Figure 10. Quantum efficiency vs. applied bias voltage for each SCA

As a function of bias, on the right side of the graph, there is a sharp decline in responsivity, which is attributable to the applied negative voltage being too small to turn on the direct injection FET and the detector itself. The 2.85 µm cutoff detector yielded significantly lower responsivity and quantum efficiencies compared to the 3.3 and 4.2 µm cutoff detectors. The 4.2 µm cutoff detector required the strongest reverse bias voltage for turn-on, and it also displayed a less abrupt turn-on point as the reverse bias increased. This suggests the possible existence of a valence band offset (VBO), which appears when the valence band in the barrier is not equal to the valence band in the absorber region, creating a barrier that requires stronger biasing for proper operation. This is a known issue in bulk *nBn* detectors such as the ones originally proposed by Wicks [3]. The issue

can be mitigated by using a III-V type-II superlattice (T2SL) for the absorber region, or by changing the barrier composition, allowing for the tuning of the valence band, eliminating the existence of the VBO [10].

The quantum efficiency as shown in Figure 10 follows the shape of its counterpart responsivity curve. Judging the performance of the SCAs based on the responsivity and quantum efficiency alone may lead to the assumption that increasing the applied negative bias would yield better performance; however, this would not take into account the increase in dark current that comes with stronger biasing, as will be seen in subsequent sections.

4.2 Responsivity and Quantum Efficiency vs. Temperature

The measured responsivity curves as a function of operating temperature are shown below in Figure 11. These data were collected at the optimal bias determined for each SCA under the nominal operating conditions of a 150 K temperature and a 10 millisecond integration time.

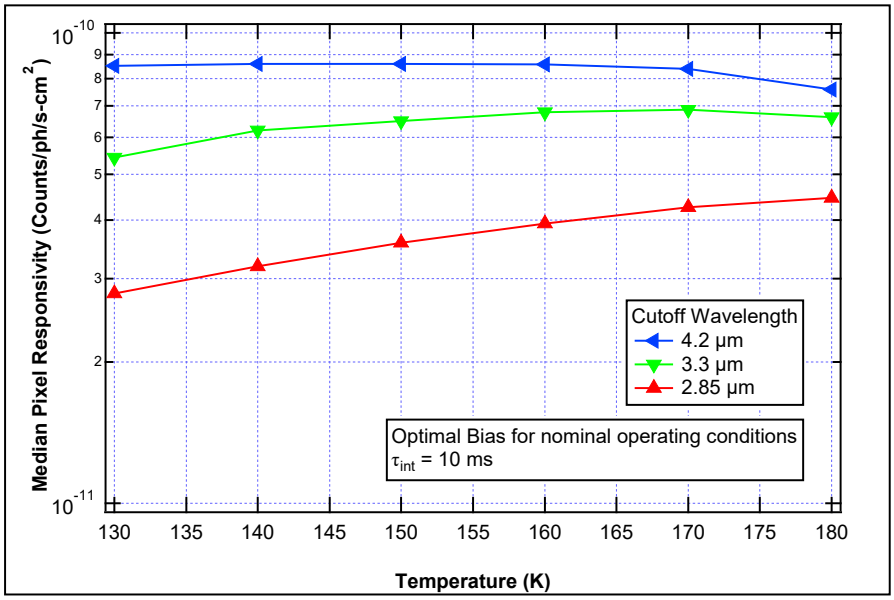

Figure 11. Median pixel responsivity vs. temperature for each SCA

Using the responsivity as a function of operating temperature, the quantum efficiency as a function of operating temperature for every SCA was also calculated according to equation 2.1. The results are displayed below in Figure 12.

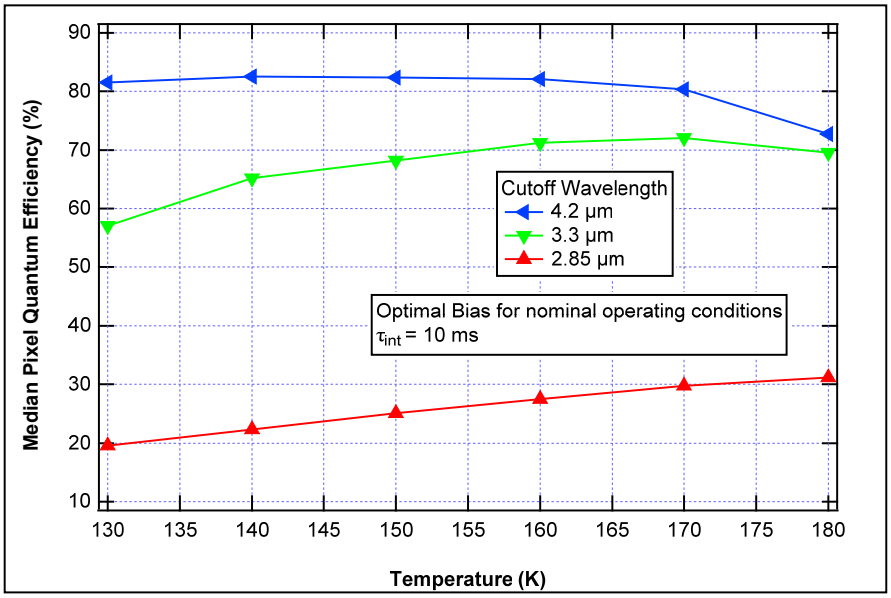

Figure 12. Median pixel quantum efficiency vs. temperature for each SCA

As a function of temperature, Figures 11 and 12 show that responsivity and quantum efficiency have a small bell shape for the 4.2 μm and 3.3 μm cutoff SCAs, but for the 2.85 μm cutoff SCA the responsivity and quantum efficiency steadily increases with temperature over this range. This is likely as a result of the diffusion length of the minority carriers increasing with temperature for the 2.85 μm cutoff SCA, due to an increase in hole mobility. Casias *et al.* showed in 2019 the mobility of minority hole carriers increasing as a function of temperature in a near infrared (NIR) InAs/InAsSb T2SL, indicating that a similar trend may account for the increase in quantum efficiency observed for the 2.85 μm cutoff SCA [11]. The effect that temperature has on the quantum efficiency and responsivity of an SCA is dependent on the minority carrier recombination mechanisms that are dominant.

4.3 Dark Current

The median pixel dark current density was obtained from measurements of output versus integration time at very low irradiance, E_q = 1.0 x 10^9 ph/s-cm^2. The measured dark current varied as a function of operating temperature as shown in Figure 13. The dark current values for all three SCAs are shown for a similar bias voltage of -0.48 V. While this is not necessarily the optimal bias voltage for each SCA, -0.48 V was determined to be adequate for all three SCAs to operate at low irradiance levels and compare their relative dark current levels.

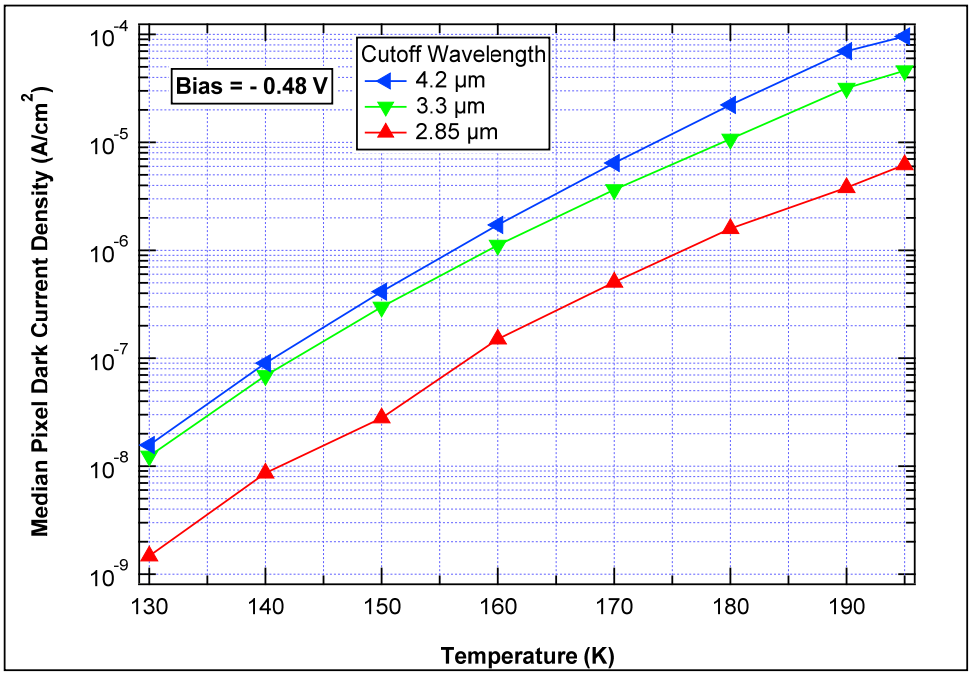

Figure 13. Median pixel dark current density vs. temperature for each SCA

Varying the applied detector bias at the nominal operating temperature of 150 K yields the median pixel dark current density plot displayed in Figure 14.

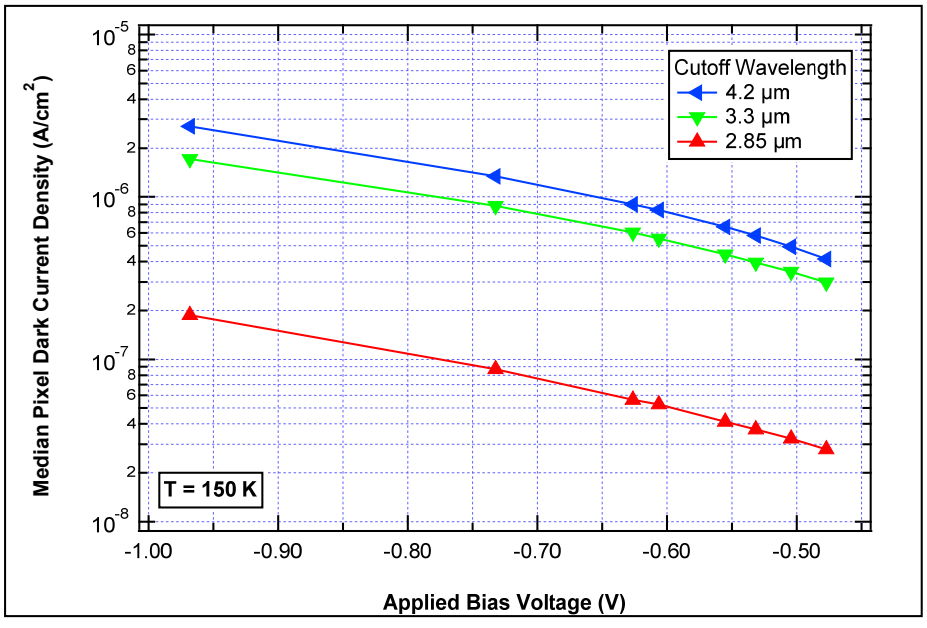

Figure 14. Median pixel dark current density as a function of applied bias voltage

It can be seen that the longer cutoff wavelength SCAs display significantly higher dark current than the shorter cutoff SCAs, which is attributable to their relatively narrower band gaps. Figure 14 shows the dark current increases for all three measured SCAs with increasing reverse bias. As the reverse bias increases, the width of the depletion region increases, leading to an increase in depletion current as can be seen in Eq. 1.1. This behavior likely suggests the dark current of each detector is dominated by generation-recombination dark current at this operating temperature. Figure 13 shows that the dark current increases with increasing temperature, due to an increase carrier density and recombination processes.

4.4 Activation Energy

Plotting the dark current density versus inverse temperature and extracting the activation energies as described in section 2.6, yields the values shown in Figure 15. The exponential fit is shown with dashed lines, and the chi-squared values for the fit are reported in order to provide information about the quality of the fit.

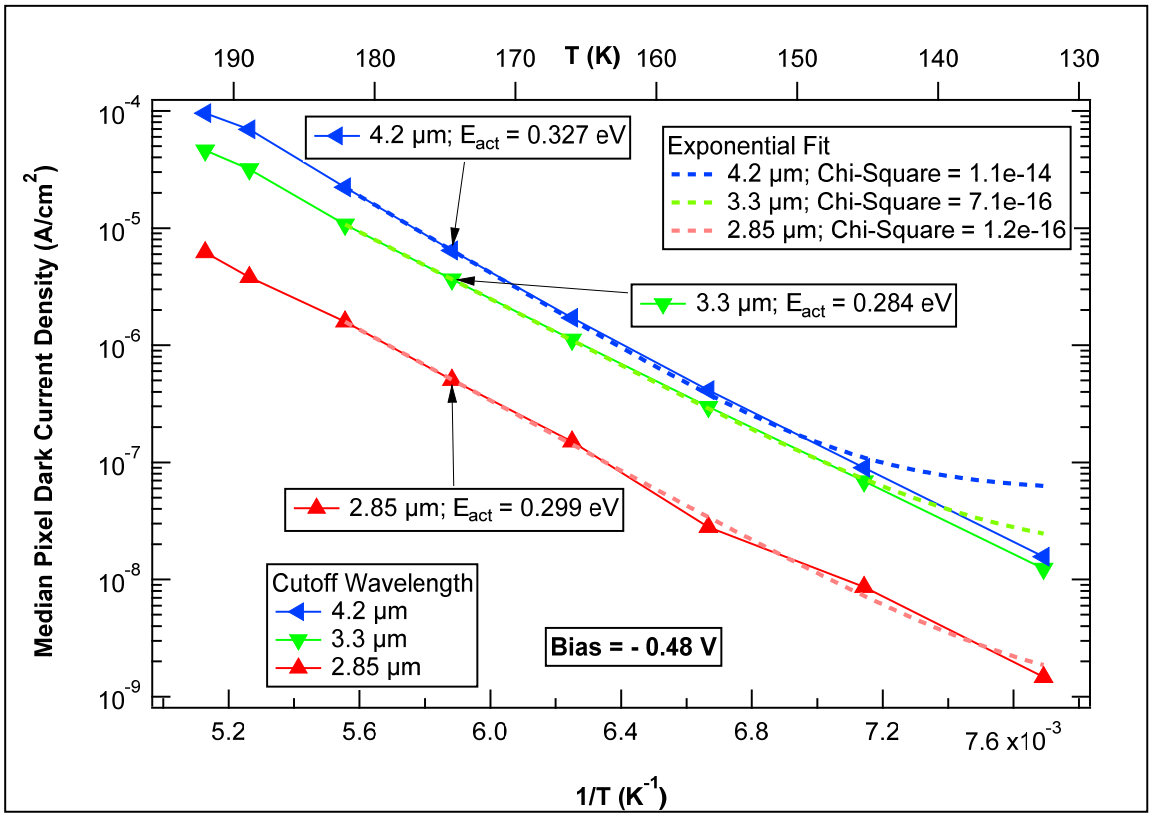

Figure 15. Activation energy from Arrhenius dark current analysis.

The activation energies computed for the 2.85 µm, 3.3 µm and 4.2 µm cutoff wavelengths were 0.299 eV, 0.284 eV and 0.327 eV respectively. For the 2.85 µm and 3.3 µm SCAs, the activation energy is lower than the band gap calculated in section 4.6, but for the 4.2 µm cutoff SCA, the results show an activation energy that is slightly higher than the band gap.

A comparison of the activation energies to the respective band gaps of the detector are shown below in Table 1.

Table 1. Band gap and activation energy comparison

λ_c(μm)	Band gap (eV)	E_{act} (eV)	E_{act} as percent of band gap (%)
2.85	0.435	0.299	69
3.3	0.376	0.284	76
4.2	0.295	0.327	111

The activation energy as a percentage of the band gap can yield information regarding the dominant dark current process. The closer the activation energy is to 50% of the band gap, the more the dark current processes are dominated by generation-recombination in the depletion region of the detector. For activation energies close to the band gap, the dark current process is dominated by recombination processes in the quasi-neutral absorber region of the detector. Therefore, the results here suggest the existence of a non-zero depletion width at the barrier junction, which allows for depletion currents to exist in the higher band gap *nBn* detectors with cutoff wavelengths of 2.85 μm and 3.3 μm. Furthermore, the existence of a higher number of mid gap trap states in the lower cutoff detectors can be inferred due to the lower quantum efficiency of the detectors [12]. As the number of mid gap trap states increases, the carrier lifetime is reduced, decreasing the diffusion length of the carriers and thus the quantum efficiency of the detector. Therefore, the results indicate the combined effects of a non-zero depletion width and an increase in mid gap trap states for the lower cutoff detectors. Defects in the detector material can be due to the lattice being mismatched to the substrate, or due to absorbing layers being grown as strained layer superlattices [5].

For the 4.2 μm cutoff SCA, the activation energy is higher than the band gap of the detector. This points to the existence of a valence band offset, creating a mismatch between the valence band of the absorber and the valence band of the barrier, blocking the flow of minority hole carriers, which are the photogenerated signal carriers in an *nBn* detector. This is consistent with the results of section 4.1, which show that the 4.2 μm cutoff SCA requires stronger biasing for nominal operation. It is possible that these results are also impacted by the poor injection efficiency of the DI unit cell under low irradiance conditions and low R_0A products, especially for the 4.2 μm cutoff SCA, as low band gaps lead to detectors with low R_0A products.

4.5 Rule ’07: Dark Current Comparison to HgCdTe Photodiodes

Using the procedure outlined in section 2.7, the expected dark current density for HgCdTe photodiodes was calculated across the temperature range at which the *nBn* FPAs were characterized. Figure 16 shows the measured dark current density of the *nBn* detectors in conjunction with the calculated values for HgCdTe photodiodes.

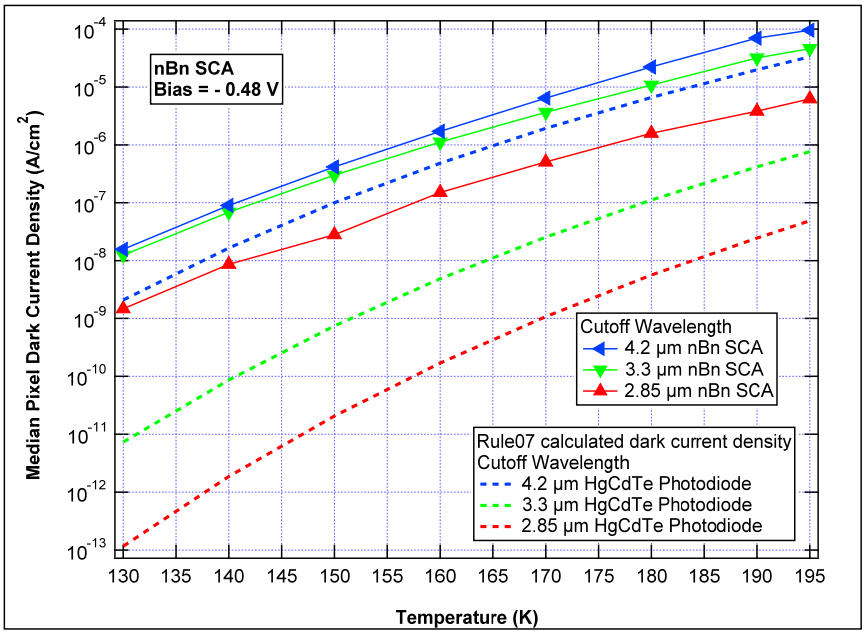

Figure 16. Rule '07 comparison of *nBn* dark current to calculated HgCdTe photodiode dark current density.

In order to better observe the divergence of the *nBn* dark current density from the calculated HgCdTe dark current density, the ratio of *nBn* dark current density to HgCdTe calculated dark current density is computed and plotted in Figure 17.

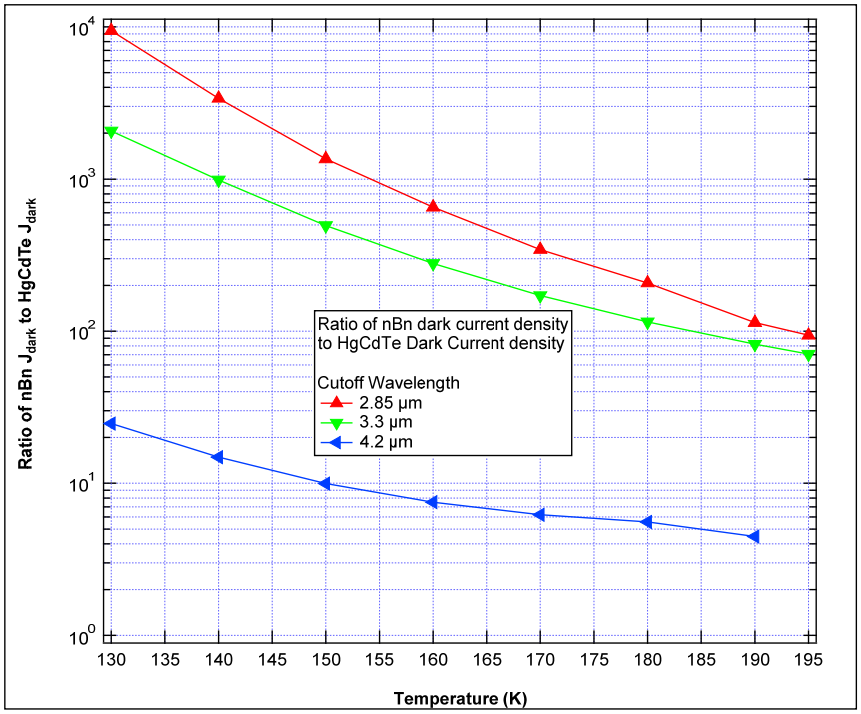

Figure 17. Rule ’07 Ratio of *nBn* Dark Current Density to HgCdTe calculated Dark Current Density.

The *nBn* detectors consistently display higher dark current compared to their HgCdTe photodiode counterparts. However, it can be seen from the trends in the data that the *nBn* detectors approach the HgCdTe level of performance as the temperature increases and as the detector cutoff wavelength is increased.

The stronger underperformance shown by the lower cutoff wavelength detectors can be explained by the significant depletion current component, resulting in overall higher dark current. Since the 4.2 µm detector does not have a significant depletion current component, it’s performance more closely matches its HgCdTe counterpart. The reason for the reduction in underperformance of the *nBn* detectors as a function of temperature is due to the diffusion current becoming more dominant at higher temperatures, causing the depletion dark current to become a less significant component of the overall dark current.

The different detectors show varying degrees of convergence to Rule ‘07 as a function of temperature. The 2.8 μm cutoff *nBn* displays dark current approximately four orders of magnitude higher than its HgCdTe counterpart at the lowest operating temperature, 130 K. However, at the highest operating temperature, the dark current displayed by the 2.8 μm cutoff *nBn* is only approximately two orders of magnitude higher than its HgCdTe counterpart. This indicates two orders of magnitude improvement in terms of its relative performance compared to its HgCdTe counterpart across the measured temperature range. On the other hand, the 4.2 μm nBn detector displays approximately 25 times higher dark current compared to its HgCdTe counterpart at the lowest operating temperatures, while at the highest measured temperature it is only approximately 4 times larger than its HgCdTe counterpart. This indicates an improvement in relative performance compared to its HgCdTe counterpart of only 6x for the 4.2 μm cutoff *nBn* across the temperature range measured. The level improvement in relative performance is proportional to the level of depletion current displayed by the detectors, meaning, the more dominant the depletion current is, the larger the improvement in relative performance is as a function of temperature, as the depletion current becomes less dominant at higher temperatures. These results are consistent with the activation energy and band gap calculations displayed in Table 1.

4.6 Noise Models

Using noise data as a function of incident irradiance levels, noise models for every cutoff wavelength were created in order to showcase how the noise contributions change as a

function of irradiance. Figures 18, 19 and 20 show the noise contributions for the 2.85 µm, 3.3 µm and 4.2 µm cutoff SCAs respectively.

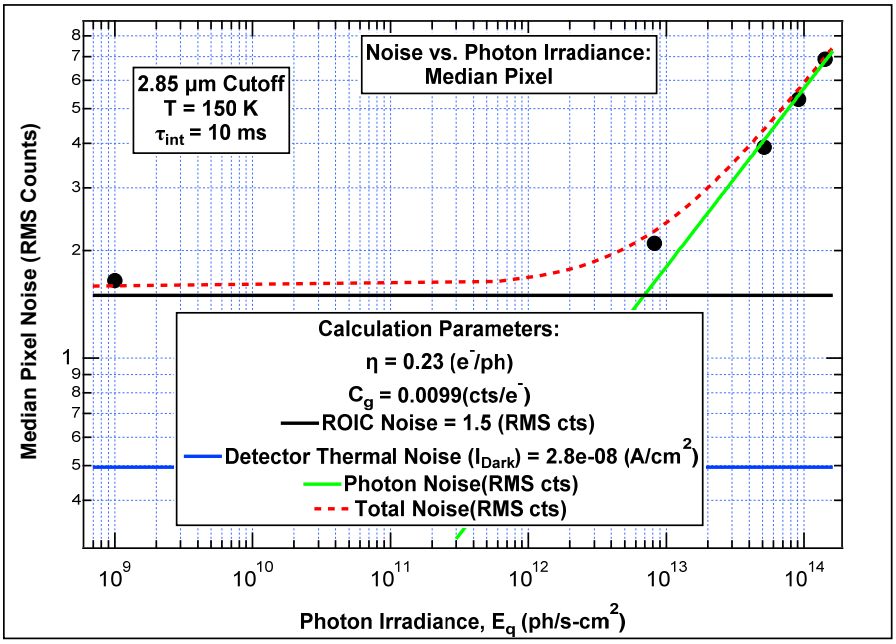

Figure 18. Noise model for 2.85 µm cutoff part as a function of irradiance

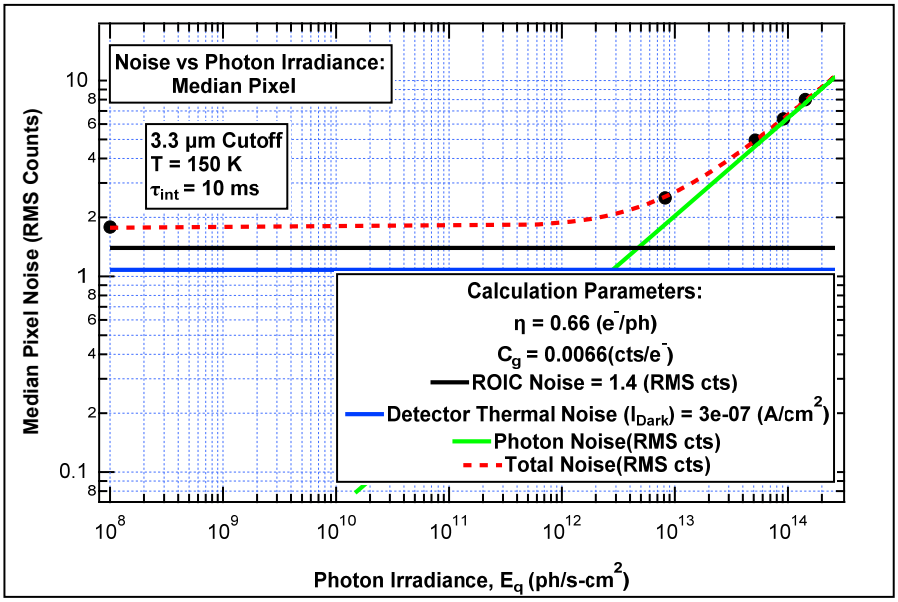

Figure 19. Noise model for 3.3 µm cutoff part as a function of irradiance

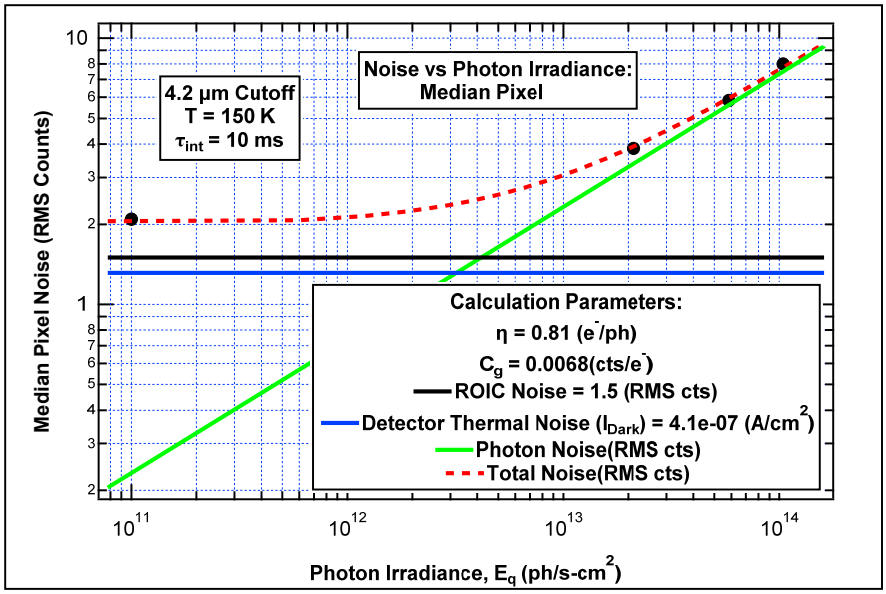

Figure 20. Noise model for 4.2 µm cutoff part as a function of irradiance

For the 2.85 µm cutoff SCA, the ROIC noise dominates for low irradiance levels. For the 3.3 µm and 4.2 µm SCAs, the detector thermal noise is a significant component compared to the 2.85 µm cutoff SCA, however the ROIC noise remains the larger factor at low photon irradiances. The larger the cutoff wavelength, the more significant the contribution of thermal noise is to the total noise. For all cutoff wavelengths measured, as the irradiance is increased, the photon noise becomes the dominant source of noise, with the detector approaching BLIP operation.

4.7 Noise Equivalent Irradiance

Figure 21 shows the median pixel noise equivalent irradiance as a function of incident irradiance, measured at the nominal operating conditions of 10 milliseconds integration time and 150 K operating temperature. These data are reported at the optimal bias determined for every SCA at 150 K. Appended to the plot is the background limited

infrared photodetector (BLIP) line which shows the theoretical noise floor due to photon noise of an ideal photodetector with 100% quantum efficiency.

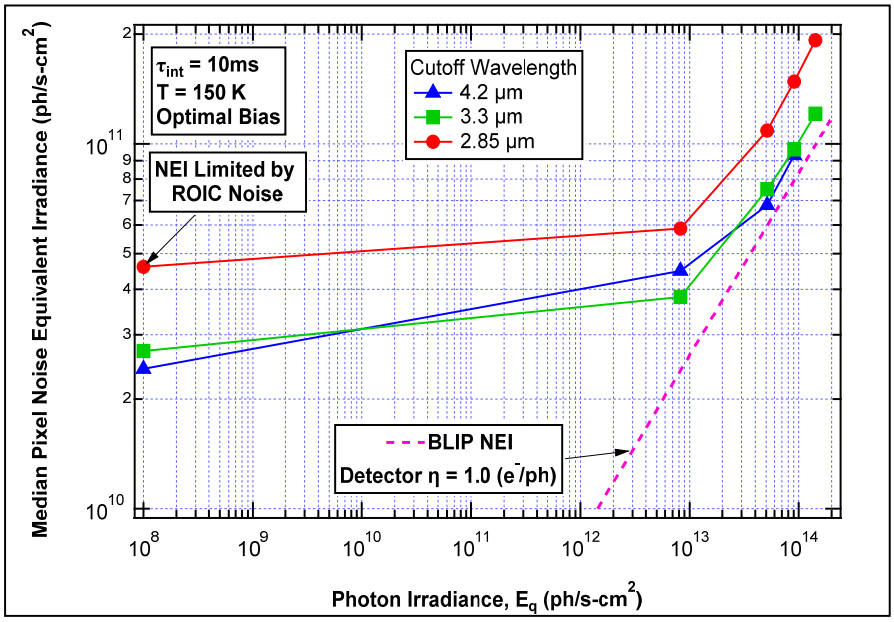

Figure 21. Median Pixel Noise Equivalent Irradiance as a function of Photon Irradiance

The noise equivalent irradiance as a function of applied detector bias at the nominal operating temperature of 150 K and high irradiance levels is presented below for each SCA in Figure 22. Note that the 4.2 µm cutoff SCA is measured at a slightly lower irradiance than the other SCAs, thus making a direct comparison of NEI values between the different SCAs difficult. However, the manner in which these values change with respect to the applied detector bias is still readily observable from the data.

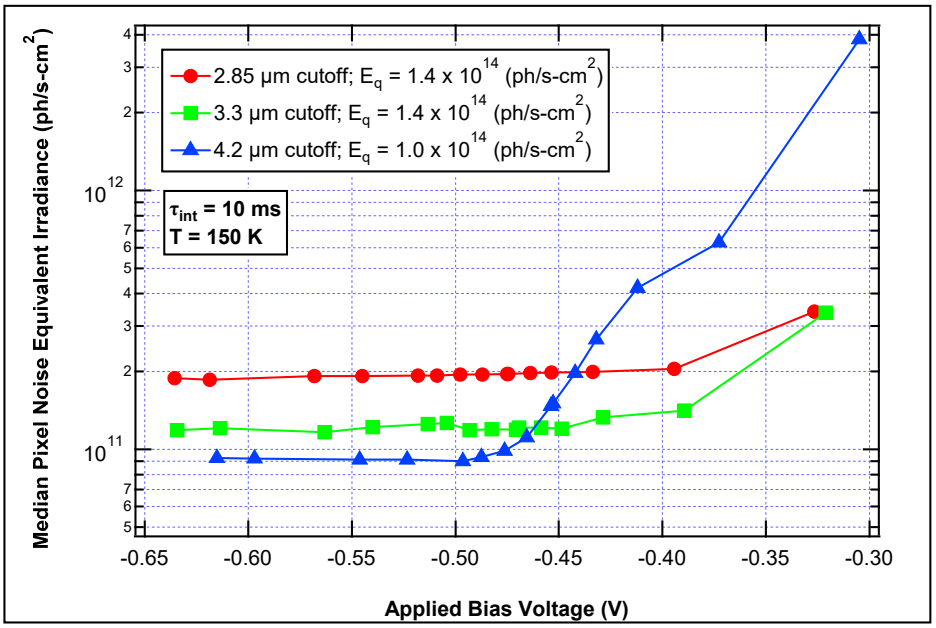

Figure 22. Median Pixel Noise Equivalent Irradiance as a function of Applied Bias Voltage

The median pixel noise equivalent irradiance at the highest available irradiance levels for each SCA is displayed in Figure 23 as a function of temperature.

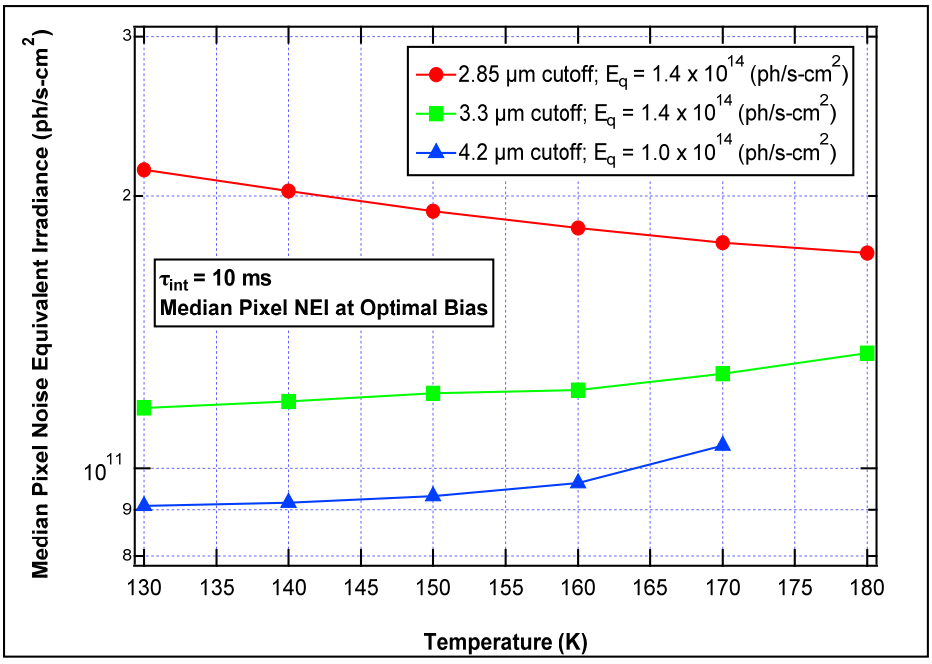

Figure 23. Median Pixel Noise Equivalent Irradiance at high irradiance as a function of Temperature

From the NEI vs. Irradiance plot shown in Figure 21, it is apparent that the longer cutoff SCAs exhibit lower NEI, and therefore higher detectivity. This is because the increase in responsivity and quantum efficiency that was observed for the longer cutoff wavelength SCAs more than offsets the increase in dark current, thus overall lowering the noise equivalent irradiance and increasing the detectivity compared to the shorter cutoffs SCAs.

The effect that the applied detector bias has on NEI can be observed from the NEI vs. applied detector bias plot as shown in Figure 22. It is readily apparent that the 4.2 µm SCA requires a negative bias higher in magnitude than the 2.85 µm and 3.3 µm cutoff SCAs, as was discussed previously. At high irradiance values, the 2.85 µm cutoff SCA

has the widest available operating range, with the NEI staying relatively stable down to voltage magnitudes as low as 0.4 Volts. The 3.3 μm cutoff SCA also displays a relatively wide operating range, with the NEI staying flat for voltage values as low in magnitude as 0.45 Volts. The 4.2 μm SCA, however, starts showing deterioration in NEI for voltage magnitudes lower than 0.5 Volts in high irradiance conditions.

From the NEI vs. operating temperature measured at high irradiance levels, shown in Figure 23, it is apparent that for the 2.85 μm cutoff, the NEI is decreasing with temperature. This is due to the quantum efficiency of the detector increasing with temperature, while the noise contribution from dark current remained insignificant compared to the other noise sources. For the 3.3 μm and 4.2 μm cutoffs, the NEI increased with temperature. This is due to the dark current becoming a more significant noise factor as temperature increases, even at higher irradiance levels.

Chapter 6

Summary

The performance of the SCAs outlined in this paper follows a constant trend, where the longer cutoff SCAs outperform the shorter cutoffs. This applies to most metrics described in this paper, including responsivity, quantum efficiency, dark current, and NEI. The only metric that does not follow this trend is the operating range for applied detector bias, which shows an opposite correlation, where the shorter the cutoff wavelength, the lower the magnitude of the applied detector bias can be before causing deterioration in the NEI characteristics. The stronger biasing requirement for the long cutoff detectors is likely due to a valence band offset defect, which could be reduced by matching the valence band of the barrier to the valence band of the n-type material using. For the 2.85 μm cutoff SCA, the quantum efficiency increased with temperature, suggesting an increase in minority carrier mobility and hence diffusion length. This resulted in an improvement in sensitivity as a function of temperature for the 2.85 μm cutoff SCA.

In terms of optical response and noise characteristics, the III-V *nBn* detectors characterized in this work underperform the state-of-the-art HgCdTe photodetectors, which display quantum efficiencies of over 90% and dark current densities generally predictable by the Rule ‘07 heuristic. With a quantum efficiency of 25% at the operating temperature of 150 K for the 2.85 μm cutoff SCA, it is likely that the detector quantum

efficiency is diffusion limited due to low carrier lifetime. This supposition is supported by the Arrhenius analysis which showed the activation energy approaching Eg/2 for the 2.85 μm cutoff *nBn* SCA, indicating that the dominant source of dark current was SRH recombination processes in the depletion region of the detector. These results indicate that the *nBn* detectors display nonideal characteristics, such as the existence of a depletion region at the barrier interface and a large number of mid gap trap defects, which serve to lower the carrier lifetime and increase the dark current density.

The comparison to Rule '07 HgCdTe photodiodes indicated dark current higher by as much as four orders of magnitude at 130 K for the 2.85 μm cutoff detector, while the 4.2 μm detector showed a dark current only 4.5x higher at 190 K. A similar dark current comparison between III-V *nBn* detectors and HgCdTe photodiodes was reported in 2014 by Rogalski and Martyniuk [14]. The results indicated that at an operating temperature of 150 K, the III-V *nBn* detectors displayed approximately 30x higher dark current then the Rule '07 heuristic for a cutoff wavelength of 5 μm, and approximately 10x higher dark current for a cutoff wavelength of 10 μm. Compared to the results from 2014, the 4.2 μm detector characterized in this work displayed a dark current density approximately 10x higher than Rule '07, indicating a 3x relative improvement compared to the 5 μm detectors from 2014. While the *nBn* detectors still underperform traditional HgCdTe photodiodes, the results indicate an ongoing improvement in the technology, which may serve to further reduce the performance discrepancy in future years as defects are eliminated. For future characterizations of dark current, it is recommended to use a CTIA unit cell amplifier as it is better suited for low irradiance conditions, in order to reduce possible artifacts introduced by the ROIC.

REFERENCES

[1] John E. Hubbs, “Infrared Focal Plane Arrays”, *SPIE Short Courses*, 2019.

[2] P. Norton, “Handbook of Optics, 2nd Edition, Vol. I, Chapter 15”. *McGraw-Hill, INC* (1995).

[3] Maimon, S and Wicks, G.W., “nBn detector, an infrared detector with reduced dark current and higher operating temperature”, *Appl. Phys. Lett.* 89, 151109 (2006).

[4] John E. Hubbs, Chris Morath, Vince Cowan, Paul W. Marshall, “Comparison of the Proton Radiation Response of HgCdTe Focal Plane Array Technologies to an III-V *nBn* MWIR Focal Plane Array”, *2014 Meetings of the MSS Specialty Groups on Infrared Detectors* Gaithersburg, MD (2014).

[5] G.W. Wicks, C.P. Morath, “Diffusion current characteristics of defect-limited nBn mid-wave infrared detectors”, *Appl. Phys. Lett*, vol. 106, 173505 (2015).

[6] D.K. Schroder, "Carrier lifetimes in silicon," *IEEE Transactions on Electron Devices, 44(1)*, January 1997.

[7] Victor D. Pepel “Radiometric characterization of Extended-SWIR and MWIR III-V nBn Infrared Focal Plane Arrays”*, 2019 Meeting of the MSS Specialty Groups on Infrared Detectors*, Orlando, Florida (2019).

[8] John E. Hubbs, “Infrared FPA Testing and Characterization”, *UCSB Extension Course* (2019).

[9] W.E. Tennant, ““Rule 07’’ Revisited: Still a Good Heuristic Predictor of p/n HgCdTe Photodiode Performance?”, *Journal of ELECTRONIC MATERIALS*, Vol. 39, No. 7(2010).

[10] J. R. Pedrazzani, D. E. Sidor, and G. W. Wicks G. R. Savich, "Benefits and limitations of unipolar barriers in infrared photodetectors," *Infrared Physics and Technol.*, vol. 59, pp. 152-155, 2013.

[11] Lilian K. Casias, “Transport in Mid-Wavelength Infrared (MWIR) p- and n-type InAsSb and InAs/InAsSb Type-II Strained Layer Superlattices (T2SLs) for infrared detection”, *University of New Mexico* (2019).

[12] Ming Liu, “Photonic Devices”, *Cambridge University Press* (2005).

[13] Olson, Benjamin Varberg, Kadlec, Emil Andrew, Kim, Jin K., Klem, John F., Hawkins, Samuel D., Shaner, Eric A., and Flatte, Michael E. “Intensity- and temperature- dependent carrier recombination in InAs/In(As1-xSbx) type-II superlattices.” United States: N. p., 2015. Web. doi:10.1103/PhysRevApplied.3.044010.

[14] Piotr Martyniuk, Antoni Rogalski, "Performance comparison of barrier detectors and HgCdTe photodiodes," *Optical Engineering, 53(10)*, November 2014.